CCFE
CULHAM CENTRE FOR FUSION ENERGY

UK Atomic Energy Authority

UKAEA-CCFE-PR(23)133

R. Thomas, D. Bowden, D. Lunt, D. Stewart, M. Preuss

High compressive loading performance of a complex multi-phase hard-facing alloy explained through a super-elastic silicide phase

High compressive loading performance of a complex multi-phase hard-facing alloy explained through a super-elastic silicide phase

R. Thomas, D. Bowden, D. Lunt, D. Stewart, M. Preuss

This is a preprint of a paper submitted for publication in
Acta Materialia

High compressive loading performance of a complex multi-phase hard-facing alloy explained through a super-elastic silicide phase

Rhys Thomas[1], David Bowden[1,2], David Lunt[1,2], David Stewart[3], and Michael Preuss[1,4]

[1] Department of Materials, The University of Manchester, Oxford Road, M13 9PL, UK.
[2] United Kingdom Atomic Energy Authority, Culham Science Centre, Abingdon, Oxon, OX14 3DB, UK
[3] Rolls-Royce Plc, PO Box 31, Derby, DE24 8BJ, UK.
[4] Department of Materials Science and Engineering, Monash University, Clayton, VIC 3800, Australia.

Abstract

Hard-facing alloys in nuclear applications must remain resistant to deformation and wear, whilst also minimising transmutation to problematic elements during service. To this end, the Fe-based alloy RR2450 has been developed to potentially replace Co-based hard-facing alloys. RR2450 is a complex multi-phase stainless steel alloy showing an unusually high strength. In order to understand the possible root cause for such favourable mechanical behaviour, the phase specific response was recorded in this materials during mechanical loading using neutron diffraction and electron microscopy based high-resolution digital image correlation in combination with electron backscatter diffraction (EBSD). The detailed analysis shows that despite the high-volume fraction of hard phases expected to impose constraint on the relatively soft ductile ferrite and austenite phases, the latter still deform plastically first. The in-situ loading experiment using neutron diffraction revealed that the hard π-ferrosilicide phase assumes large elastic strains while at the same time showing significant diffraction peak broadening. Additional electron microscopy-based strain mapping on compressed samples confirmed an almost pure elastic response of the π-ferrosilicide phase. The possible effect of lattice cell angular distortion of the π-ferrosilicide phase on diffraction peaks was modelled using crystal structure analysis, demonstrating that small changes (<1°) in angular lattice cell parameters can account for the apparent broadening observed by neutron diffraction. Such reversible super-elasticity by angular distortion of the unit cell is expected to provide a significant pull-back effect during unloading resulting in improved galling wear resistance, an important performance factor for hard-facing alloys intended for nuclear applications.

1. Introduction

Pump and valve seat components in a pressurised water reactor (PWR) require hard-facing alloys that remain resistant to deformation and severe wear phenomena, as well as provide excellent aqueous corrosion performance. One of the key design criteria for the hard-facing alloys here is a high galling resistance, which is a type of cold welding phenomena that can occur when two metallic components remain compressed for some time [ref], which could lead to seizure of components. To date, the alloys of choice for these application are Co-based alloys such as Stellite 6, which maintain high levels of wear and corrosion resistance within the temperature range of up to 300 °C [1]. However, Co is a problematic element within a nuclear plant, suffering from transmutation to ^{60}Co, which produces highly energetic γ rays with a half-life slightly in excess of 5 years. This poses a risk to plant personnel and impedes maintenance and decommissioning activities [2].

RR2450 is one of several new Co-free hard-facing alloys that are currently under development. It offers a low-activation hard-facing material solution and is a complex multi-phase high carbon Fe-based alloy, containing ductile austenite (γ) and ferrite (δ), as well as carbide (M_7C_3) and carbonitride ((Nb,Ti)C,N) phases. Studies of the RR2450 alloy have also revealed the presence of a silicide phase (named π-ferrosilicide), with a $P2_13$ crystal structure, constituting up to 23% of the microstructure [3]. The π-ferrosilicide grains form from δ-ferrite after cooling from 920 °C, retaining a strong orientation relationship to the parent δ-ferrite grain [3,4]. In-situ loading experiments using neutron diffraction highlighted relatively early load partitioning to the π-ferrosilicide phase, as austenite and ferrite yielded first, suggesting that the π-ferrosilicide phase contributes greatly to the hard-facing properties of this alloy [3]. However, the micromechanical behaviour of an alloy with two relatively soft ductile matrix phases (δ and γ), a hard matrix phase (π) and two hard precipitate phases (M_7C_3 and (Nb,Ti)C,N) is expected to be highly complex. In particular, there is a great interest in better understanding the micromechanics of the relatively poorly known π-ferrosilicide phase within this multiphase alloy due to its expected contribution to high wear resistance and its crystallographic relationship with the δ-ferrite [3,4] suggesting reduced decohesion from the matrix compared to carbide and carbonitride precipitates.

There are a number of different experimental techniques that enable the study of phase specific response during mechanical loading. A well-established experimental methodology is the use of highly penetrating diffraction techniques such as neutron or high energy synchrotron x-ray diffraction. Both approaches enable one to measure the lattice strain response in the loading direction and therefore capture the phase specific elastic strain response. When mechanically loading a multiphase material, the softer phase will deform plastically first, transferring elastic strain to the harder phases. In addition to peak shifts relating to elastic strain evolution, peak broadening is also typically observed within the plastic regime, which can have various reasons to occur, though most often it is related to dislocation formation [5]. In contrast to diffraction techniques, non-contact imaging techniques in conjunction with digital image correlation enable one to measure plastic strain directly during mechanical testing. An increasingly prominent technique for measuring local plastic deformation at the sub-micron scale is high-resolution digital image correlation (HRDIC) [6], where images taken at progressive strain steps are compared to the image before deformation to produce a full-field displacement map that can be differentiated to compute the desired strain component [7,8]. These strain maps can provide sub-grain information that enable the quantification of strain localisation within individual grains and phases when

combined with orientation information collected using electron backscattered diffraction (EBSD) [9]. Hence, this experimental approach can be considered a more direct methodology, detecting slip/deformation activation in individual phases, though it is only a surface technique and phase separation requires careful analysis of the separate data sets.

Under bend testing, RR2450 has been shown to fracture before macroscopic yielding [10]. Therefore, the current study utilises compression with the aim of capturing some level of plasticity before sample failure. Compression is also the most relevant loading scenario for hard-facing alloys such as RR2450, which are located in valve seat locations and are only loaded in compression.

The aim of the present study is to correlate bulk and local strain measurements from neutron diffraction and HRDIC, respectively, within the hard-facing alloy RR2450. This is in order to shed light on the unusual combination of high compressive strength and significant elastic deformation exhibited by this alloy thorough developing a better micromechanical understanding when deforming such complex multiphase materials under loading conditions relevant to their application space. Such properties are anticipated to provide favourable galling wear-resistance in a hard-facing alloy such as RR2450. A specific question this work aims at addressing is whether the newly established π-ferrosilicide phase remains purely elastic during compression loading or if some plasticity is detected at very high stress levels. Therefore, this study provides a quantitative assessment of the suitability of the RR2450 alloy for hard-facing applications.

2. Methods

2.1. Material

The RR2450 alloy was initially gas atomised at Sandvik Osprey, UK with a target composition shown in Table 1. The powder was analysed by AMG Superalloys Ltd. using a LECO CS884 combustion infrared spectrometer (to measure C, S, O, and H), LECO ONH836 inert gas fusion spectrometer (measuring N) and Panalytical Axios wavelength dispersive X-ray fluorescence spectrometer (XRF) to measure metallic elements, providing the actual composition values shown in Table 1. After atomisation, the powder underwent hot isostatic pressing (HIP) at Hauck Heat Treatment using typical HIP parameters, in line with those used for hard-facing alloy consolidation [11].

Table 1. Target composition and actual composition (wt.%) of the RR2450 material examined in this study. Standard measurement uncertainties are indicated in parenthesis.

Alloy	**Fe**	**Cr**	**Ni**	**Nb**	**Si**	**Ti**	**C**	**N**	**O**	**Other impurities**
RR2450 target composition	Bal.	21.0	9.0	8.5	5.8	0.5	1.8	0.1 (max.)	0.02 (max)	-
RR2450 analysed (this study)	Bal.	20.5(1)	9.8(1)	6.9(1)	5.8(1)	0.6(1)	2.07(1)	0.07(1)	0.13(1)	<1.2

The RR2450 studied here has been shown to contain a triplex matrix, consisting of austenite, ferrite and π-ferrosilicide phase. In addition, precipitates in the form of M_7C_3 and (Nb,Ti)CN are found throughout the microstructure. The larger M_7C_3 (~1.5 µm diameter [12]) resides

predominantly at the interphase boundaries between the austenite, ferrite and π-ferrosilicide. The smaller (Nb,Ti)CN (~250 nm diameter [12]) is dispersed intragranularly throughout all phases in the alloy. The RR2450 phase fractions were determined using x-ray diffraction measurements combined with Rietveld analysis and are presented in Table 2 [12].

Table 2. Phase fractions (wt.%) of the RR2450 alloy measured using XRD and obtained by Rietveld analysis [12]*. Values in parentheses denote standard deviation.*

Austenite	**Ferrite**	**π-ferrosilicide**	**M_7C_3**	**(Nb,Ti)CN**
25(1)	29(3)	17(3)	14(6)	14(2)

2.2. Elastic strain analysis during in-situ compression using Neutron Diffraction

The initial uninterrupted room temperature compression loading curve for the RR2450 was obtained on a cylindrical compression sample of 8 mm Ø × 16 mm-long, using an Instron 5885H with a strain rate of 10^{-4} s^{-1}. The same specimen geometry was used for the HRDIC analysis; however, one side was ground and polished to form a flat face of ~ 1 mm across. Samples were compression loaded on the same rig in increments to loads of 718, 818, 918, 1018 and 1118 MPa, again at a strain rate of 10^{-4} s^{-1}. At each load step the sample was removed and imaged in the scanning electron microscope (SEM), before being placed back into the load frame, where loading to the next increment was applied before the imaging process was repeated.

The in-situ compression testing employing neutron diffraction was conducted on the ENGINE-X time-of-flight (TOF) neutron diffraction instrument at the ISIS facility, Didcot, UK [13]. The experimental set up is described schematically in [3]. Diffraction patterns were collected in the axial and radial directions in cylindrical samples of 8 mm Ø × 16 mm length. These were mounted in a compression rig and a 5 MPa compressive pre-load was applied before the start of the experiment. The incident beam was defined by slits to be 8 × 8 mm^2 while on the diffracting side a 4 mm collimator completed the definition of the diffracting gauge volume. The choppers were operated at 25 Hz providing a d-spacing range of 0.56 - 2.35 Å throughout the measurements. The staircase type of loading (30 minutes holding times at each loading condition for obtaining high quality diffraction data) was carried out using stress control in the nominally elastic stress regime and strain control in the stress regime where plasticity was anticipated. The loading, using a strain rate of 10^{-4} s^{-1}, was carried out in 45 MPa steps and the transition from stress to strain control took place at 410 MPa.

In order to plot the stress - phase specific elastic strain responses, the lattice parameters of the individual phases were obtained for each loading step by carrying out a Rietveld refinement using the Generalised Structure Analysis System (GSAS) software package [14] with the EXPGUI front-end [15] installed. This lattice parameters were converted to phase specific elastic strain using the conventional engineering strain equation with a_0 for each phase being the initial values before the loading started.

As unexpected peak broadening was observed for the π-ferrosilicide phase. The possible effect of lattice distortion within this phase was further investigated by performing detailed analysis of the neutron diffraction patterns using Fityk V1.2.9 [16]. This process involved fitting pseudo-Voigt (PV) peaks to best match the experimentally observed peak shapes. The π-ferrosilicide (310) peak was used for this assessment as it demonstrated a significant degree of broadening and was not

overlapped by peaks from other phases present in the alloy. VESTA V3.3.2 [17] was subsequently used to simulate the degree of unit cell angular distortion required to produce the peak shapes observed in the RR2450 π-ferrosilicide phase.

2.3. Surface strain analysis using SEM imaging and digital image correlation

An alternative method for recording phase specific strain in a multiphase material is to undertake an initial EBSD scan for phase and orientation determination of a specified area followed by imaging and digital image correlation of the same area before and after mechanical loading.

Phase and crystallographic surface mapping by EBSD

Phase and crystallographic orientation in the region of interest were conducted in a FEI Quanta 650 field emission gun scanning electron microscope (FEG-SEM) equipped with an Oxford Instruments Aztec EBSD system with a Nordlys II detector. Chemical mapping was carried out simultaneously using an Oxford Instruments energy-dispersive x-ray spectroscopy (EDS) detector. For microtexture analysis in the HRDIC regions, a step size of 0.15 μm and area of 123 × 93 μm^2 were chosen. The data were analysed using Oxford Instruments AZtecCrystal software. Due to the similar crystal structure of (Nb, Ti)CN and austenite the two phases were segmented using the Nb, Ti and C EDS signals. Any face-centred-cubic (FCC) grains with median Nb+Ti+C counts above a threshold were designated a (Nb,Ti)CN grain in the DefDAP 0.92.3 [18] Python library. The threshold was defined by considering the distribution of median Nb+Ti+C counts for all grains and noting a clear bimodal distribution.

Imaging and HRDIC

High-resolution digital image correlation (HRDIC) has been utilised to measure the strain distribution on a sub-grain scale, which combined with the EBSD analysis enabled comparing the local strains within each individual phase. For an accurate measurement, the technique requires randomly distributed speckles where the distance between the speckles is almost identical to the size of the speckle. This type of pattern was obtained using the water vapour remodelling technique [6,19], where initially a thin layer of gold layer is deposited onto the polished sample surface using an Edwards S150B sputter coater for 5 ½ min at a current of 40−45 mA. Subsequently, the sample was placed on a hot plate for 3 h at 285 °C. The remodelling process enables the thin film on the surface to agglomerate into fine gold speckles that typically have a size of 60−80 nm.

The images for HRDIC purposes were acquired in backscattered electron imaging mode in a FEI Magellan HR 400L FEG-SEM, at a working distance of 3.9 mm, an acceleration voltage of 5 kV and 0.8 nA beam current using an insertable concentric backscatter (CBS) detector. Images were captured with a horizontal field width of 37 μm at a resolution of 2048 × 1768 pixels and dwell time of 5 μs across a matrix of 20 × 20 images covering 592 × 460 μm^2. Image overlaps of 20% were used to enable easy stitching of the image matrices before digital image correlation was performed. Image matrices were obtained before deformation and after 5 subsequent stress levels and stitching was subsequently performed using the ‘Grid/Collection stitching’ function [20] with a linear blend applied between images in ImageJ version 1.52p. The set of images were aligned in terms of position and rotation by manually manipulating them, relative to the original image, using the same software. The stitched maps for the undeformed and deformed states were correlated

using LaVision DaVis 8.4. The correlation was performed relative to the image set before deformation for all deformation stages, using a sub-window size of 16 × 16 pixels and 0% overlap, equating to a spatial resolution of ~ 289 nm. The sub-window size and overlap were selected based on the noise optimisation process detailed in [21].

Combining EBSD and HRDIC data sets

Combined analysis of the HRDIC and EBSD data was carried out using the in-house developed DefDAP 0.92.3 [18] Python library. Homologous points were defined between the two datasets and an affine transformation was applied to the EBSD data to transform it to the HRDIC reference frame. This allows the HRDIC strain data to be segmented by phase and grain. In some cases, effective shear strain [6,22] was used to visualise the strain data, and is given as:

$$\gamma_{\text{eff}} = \sqrt{\left(\frac{\varepsilon_{xx}-\varepsilon_{yy}}{2}\right)^2 + \left(\frac{\varepsilon_{xy}}{2}\right)^2}, \qquad (1)$$

where ε_{xx} is strain in loading direction, ε_{yy} is strain in the in-plane transverse direction and ε_{xy} is in-plane shear. This measure interprets all strains as shear strains and is therefore a good scalar representation of local deformation at sub-micron scale since most room temperature deformation occurs by shearing of the lattice [6].

3. Results

3.1. Mechanical behaviour

The mechanical response of the material is summarised, Figure 1, in terms of both the compressive stress-strain curve (Figure 1a) and axial, phase specific elastic microstrains of the three major phases (Figure 1b, the carbide and carbonitride phases did not provide sufficienly strong diffraction peaks to be analysed) measured by neutron diffraction. From the stress-strain response the elastic modulus was estimated to be 192 GPa with deviation from linearity happening around 500 MPa. A high hardening coeficient was calculated within the relatively small total strain region with compressive stresses continuing to increase beyond 2% total strain. From linear regression of the first 8-10 points for each of the major phases (Figure 1b), the elastic moduli were estimated to be 227, 214 and 206 MPa for austenite, ferrite and the π-ferrosilicide, respectively. The compressive elastic microstrains after unloading are not plotted, but are -722, -3580 and 1665 for the austenite, δ-ferrite and π-ferrosilicide respectively. Hence, the data suggest a load transfer from γ and δ phases to the π-ferrosilicide phase within the plastic regime.

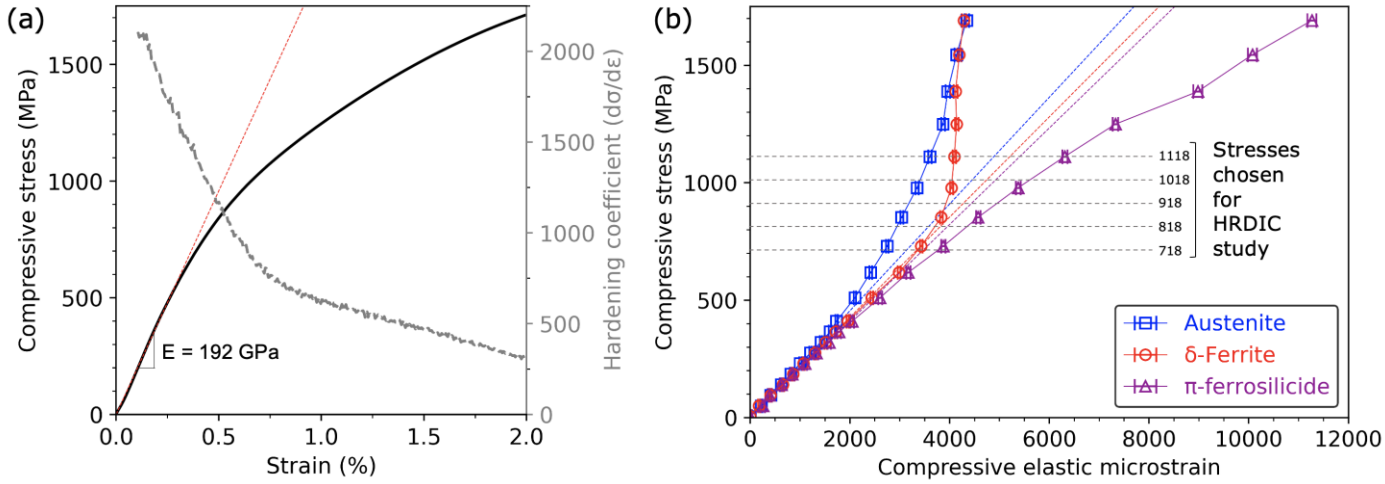

Figure 1. (a) Stress-strain curve and instantaneous strain hardening rate for RR2450. (b) Compressive elastic strain as a function of compressive stress for austenite, δ-ferrite and π-ferrosilicide in RR2450 determined by neutron diffraction.

Individual pseudo-Voigt (PV) peak fitting of the neutron diffraction data was used to determine the full width at half maximum (FWHM) of the austenite (311), δ-ferrite (211) and π-ferrosilicide (310) peaks for each deformation step and their change in comparison to the original value is plotted as a function of applied stress in Figure 2. The main observation here is that the π-ferrosilicide (310) peak undergoes significant broadening compared to either the austenite (311) or δ-ferrite (211) peaks. The π-ferrosilicide peak broadening is seen almost immediately at the start of compressive loading, i.e. before any clear evidence of plastic deformation in Figure 1a, though it becomes most significant when stresses exceed ~1300MPa.

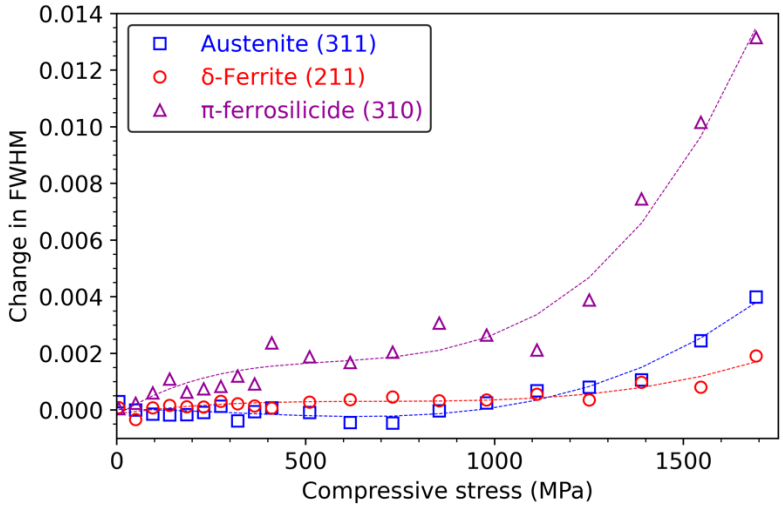

Figure 2. Change in peak FWHM of the δ-ferrite (211), austenite (311) and π-ferrosilicide (310) peaks, from the neutron diffraction data, as a function of compressive stress. A third order polynomial fit was added to guide the eye.

3.2. Local strain distribution

Figure 3 shows inverse pole figure (IPF) maps plotted for the loading direction for each phase in the material. The orientation map corresponds to the HRDIC region and indicates that in this region the relative grain size for the three main phases is largest in the austenite, then the δ-ferrite and smallest for the π-ferrosilicide. However, the π-ferrosilicide has a distinct texture in comparison to the other phases, where clusters of grains have a common orientation, which is

directly related to the orientation relationship with the prior δ-ferrite [4]. In the HRDIC region, the volume fraction of austenite and δ-ferrite is highest with lower volume fractions for the π-ferrosilicide and carbide phases. This relatively even distribution of the phase fractions between the significant phases allows us to fully investigate their interactions during deformation.

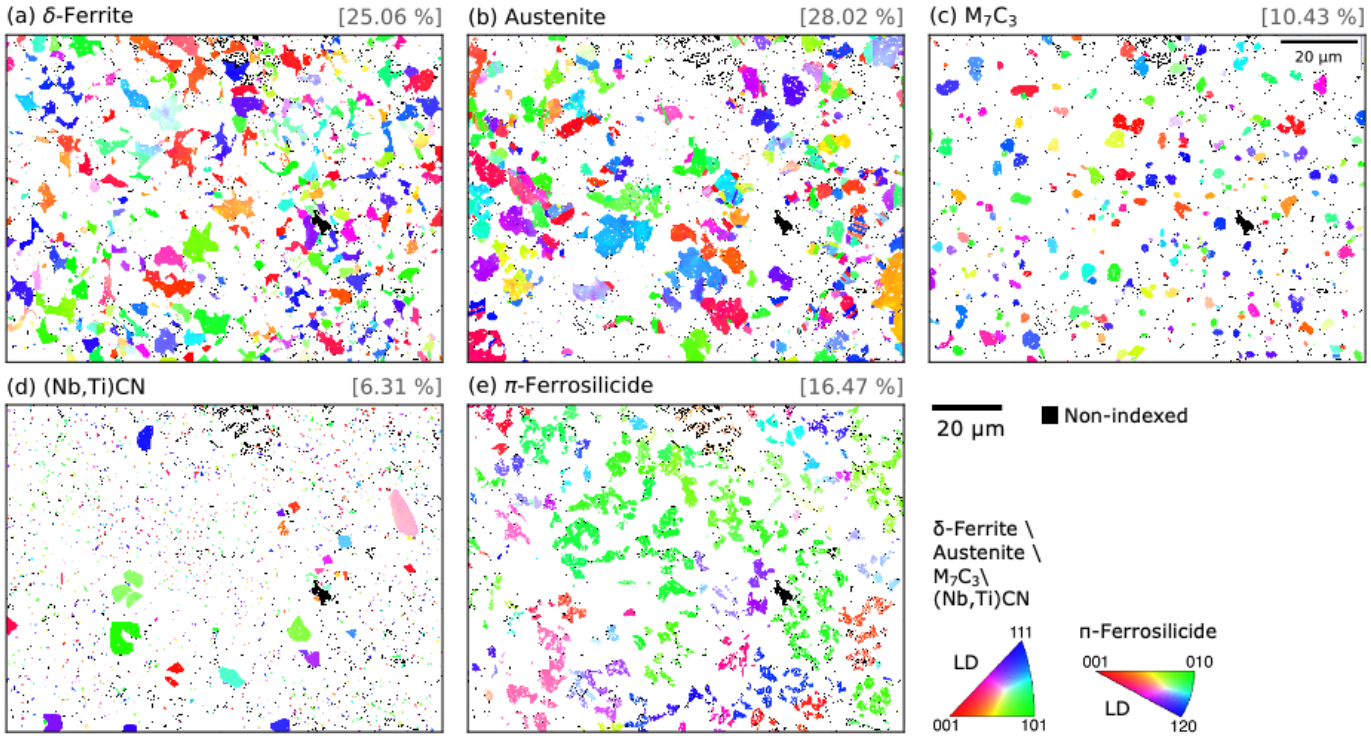

Figure 3. IPF LD maps from EBSD, for the HRDIC region, showing (a) δ-ferrite, (b) austenite, (c) M_7C_3 (d) (Nb, Ti)CN and (e) π-ferrosilicide.

By linking the phases maps of the underlying microstructure with the HRDIC data, it is possible to quantitatively assess the level of strain at each stress level for the individual phases. It can be observed that at 1118MPa (Figure 4) there is very little deformation occurring in the carbides and π-ferrosilicide. Furthermore, the regions of highest strain in these phases are typically located near phase boundaries with softer phases, suggesting some misalignment issues in the strain datasets. In contrast, the austenite and δ-ferrite exhibit significant strain localisation with very distinct slip features observed within single grains. For the austenite, the majority of grains have deformed whereas for the δ-ferrite there are several grains that appear to remain undeformed. This suggests that the austenite is easier to deform than the δ-ferrite, as not only more grains deform but slip is also more intense with many grains showing evidence of multiple slip traces. It should also be noted that the (Nb,Ti)CN phase shows little strain, even in large grains, suggesting that using the EDS signal to distinguish this phase from austenite was successful.

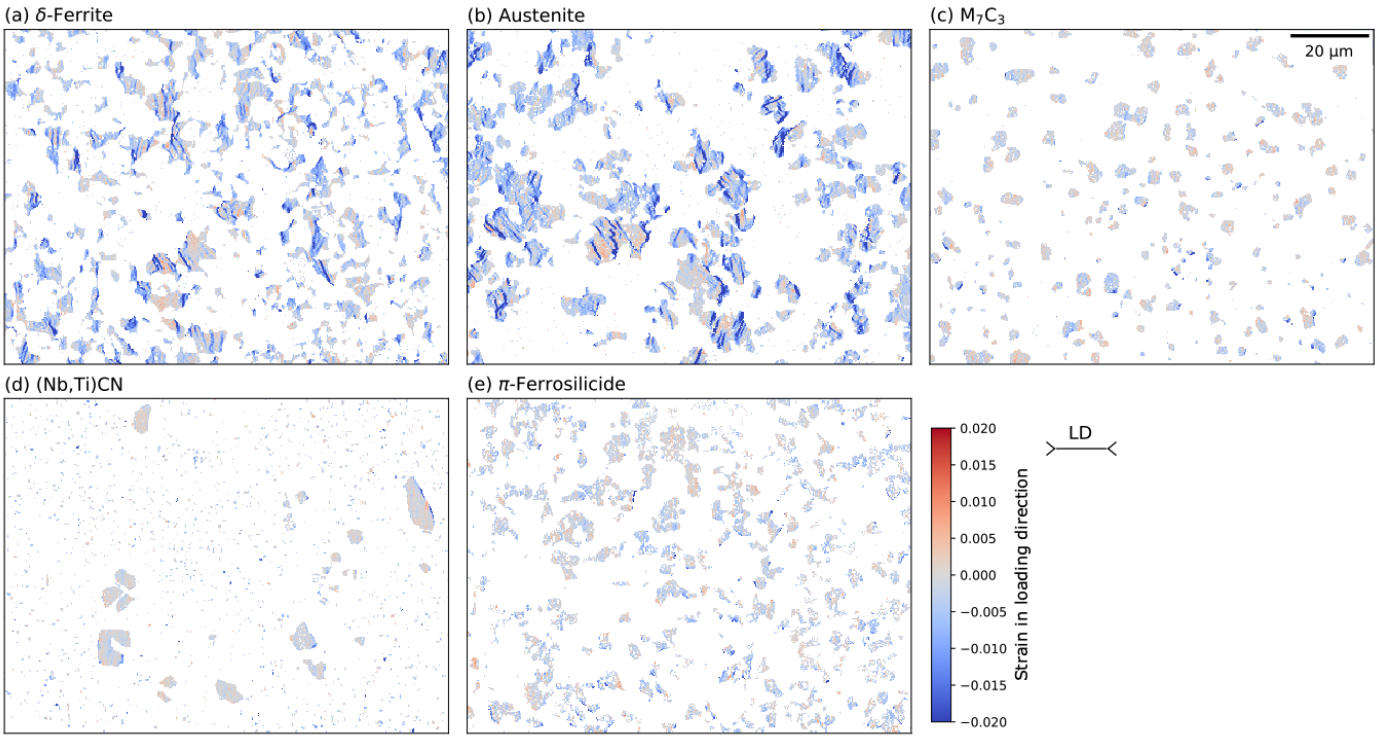

Figure 4. Strain in loading direction within the (a) δ-ferrite, (b) austenite, (c) M_7C_3 (d) (Nb, Ti)CN and (e) π-ferrosilicide within RR2450 after ex situ compressive loading to 1118 MPa.

Further quantification of the phase specific shear strain and strain in the loading direction for all load steps are shown in Figure 5. It should be noted that as individual pixels of high strain were observed near the phase boundaries for both the carbide and π-ferrosilicide phases, the strain localisation is shown in terms of raw data (solid lines) and as processed data (dashed lines) where single pixel erosion was performed. This comparison indicates that in terms of both the effective shear strain (Figure 5a) and the compressive strain (Figure 5b), the austenite and ferrite phases take up more plastic strain than the average value while the π-ferrosilicide displays less plastic strain. A more detailed analysis of the maps also revealed that for the π-ferrosilicide strains are concentrated on/near the boundaries while this is not the case for the δ-ferrite and austenite phase. This suggests that the strains for the π-ferrosilicide are likely to have been either misindexed or are a result of interactions at interphase boundaries.

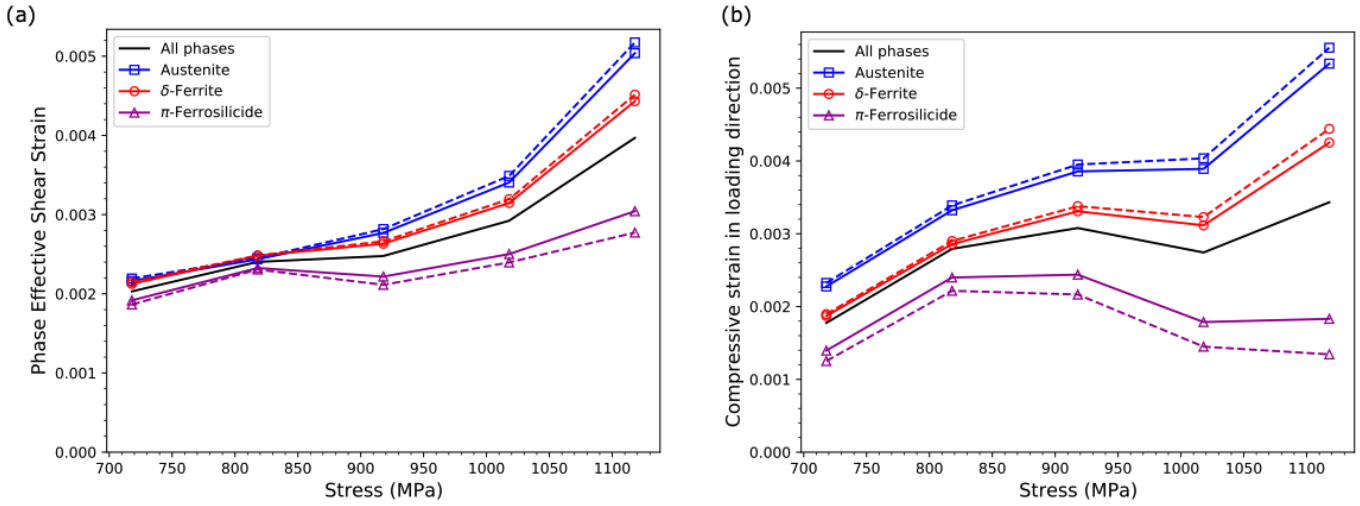

Figure 5. Plot of mean a) effective shear strain and b) compressive strain in loading direction, for each phase in the material. Solid lines represent all datapoints for each phase, whereas dotted lines denote the data eroded by one pixel to remove edge effects.

As a result of the clear slip traces observed in both the austenite and δ-ferrite, the crystal orientation relative to the slip traces in these phases is further examined in Figure 6. Firstly, the most intense slip is observed in the austenite phase with multiple slip lines of high strain and cross-slip between at least two different [111] slip planes evident from the first step and becoming more prominent at the highest stress level. Interestingly, the magnitude of the effective shear strain in slip bands in the δ-ferrite is initially similar to that in the austenite. However, at this lowest stress level, only one slip trace is clearly visible in the δ-ferrite, which is consistent with a [110] plane in the grain. Again, a comparison of the two phases at the highest stress level (1118 MPa) indicates higher effective shear strains in the austenite than the δ-ferrite.

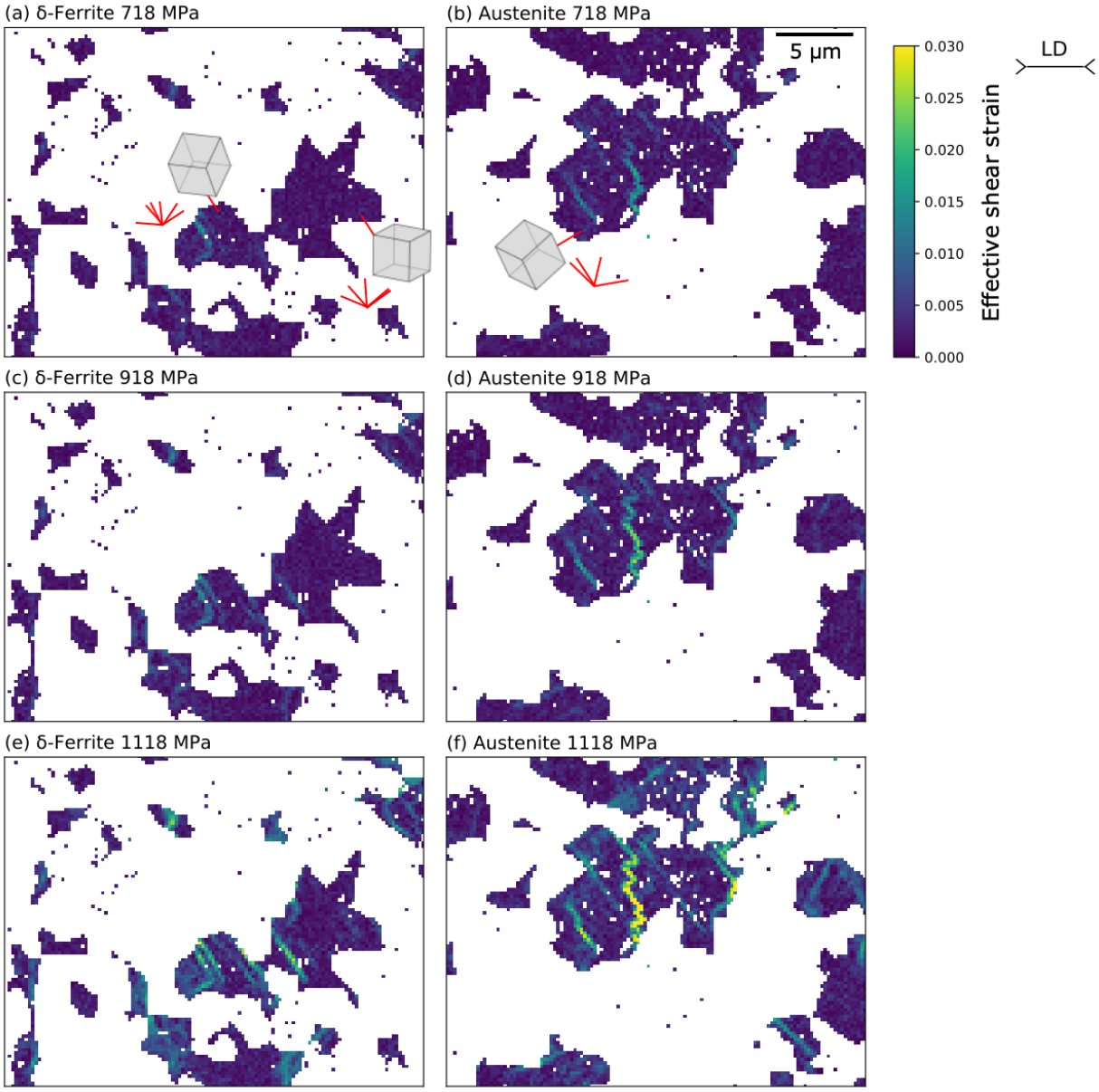

Figure 6. Effective shear strain within the (a, c, d) δ-ferrite and (b, d, f) austenite phases within a sub-region of the material after ex-situ compressive loading to 718, 918 and 1118 MPa. Unit cells are shown for grains of interest and [111] slip traces are shown for FCC austenite and [110] slip traces are shown for BCC δ-ferrite.

4. Discussion

Quantitative strain mapping was used to investigate the strain interactions in a complex multi-phase material, where capturing the deformation at multiple stress levels allows the evolution of strain in each phase to be considered. As expected from the neutron diffraction data, load transfer away from the relatively soft austenite and δ-ferrite phases was observed, suggesting that these two phases deform plastically first. Figure 1b also shows that the austenite phase deforms before the δ-ferrite phase. In contrast, the π-ferrosilicide phase picks up additional elastic strain once plasticity occurs indicating that this phase remains mainly elastic within the tested loading regime. While typically carbide and nitride phases are utilised in the design of hard-facing materials, the π-ferrosilicide phase seems to contribute significant strength to the alloy, which is likely to enhance the galling resistance of RR2450, which is one of the main design criteria for this alloy. However, analysis of the neutron diffraction data also reveals very significant broadening of the π-ferrosilicide peak (Figure 2), which is typically an indication of plasticity within a phase. The

additional HRDIC data confirm though that π-ferrosilicide acts as a hard phase within this multiphase material with no significant evidence of plasticity.

Considering that the elastic strain analysis from the neutron diffraction experiment and the plastic strain analysis of the HRDIC experiment both suggest an absence of plasticity in the π-ferrosilicide phase, the dramatic diffraction broadening observed for the (310) π-ferrosilicide peak is surprising. Hence, alternative reasons for the peak broadening were explored. The complex $P2_13$ silicide structure, and possible presence of a carbon atom within the unit cell observed in [x] suggest favourability for a possible large elastic distortion of the π-ferrosilicide phase during compression loading. First, an advanced fitting of the broadened (310) π-ferrosilicide peak was carried out by using two or three PV peaks with equal FWHM and intensities, Figure 7. Two equally sized PV peaks indicate an angular distortion of the original $P2_13$ unit cell, leading to a reduction of symmetry to produce an R3 π-ferrosilicide phase unit cell; whilst up to five peaks indicate the angular distortion of the unit cell, such that $\alpha \neq \beta \neq \gamma$ (i.e. a triclinic unit cell), in this case, regarded as the P1 space group.

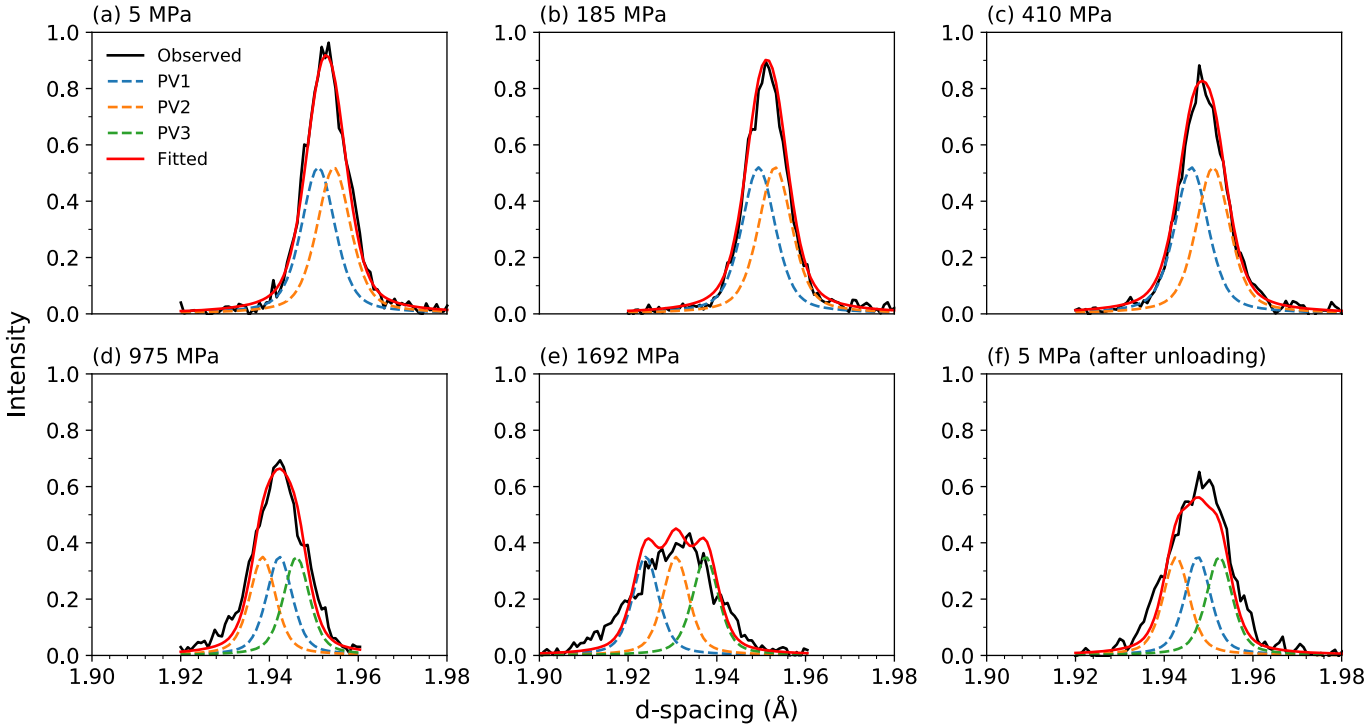

Figure 7. π-ferrosilicide (310) peak broadening as a result of elastic angular distortion of the $P2_13$ unit cell. A) $P2_13$ distortion to result in R3 symmetry such that $\alpha = \beta = \gamma = 89.82°$ at 5 MPa; B) $P2_13$ distortion to result in R3 symmetry such that $\alpha = \beta = \gamma = 89.82°$ at 185 MPa; C) $P2_13$ distortion to result in R3 symmetry such that $\alpha = \beta = \gamma = 89.75°$ at 410 MPa; D) distortion resulting in a transition to a P1 space group setting such that the range of α, β and γ values are between 90 to 89.62° at 979 MPa; E) still using P1 symmetry, α, β and γ values are between 90 to 89.34° at 1692 MPa; F) after unloading to 5 MPa there is still a residual P1 angular distortion present in the π-ferrosilicide phase unit cell such that α, β and γ are between 90 to 89.52°.

Figure 7 demonstrates that the (310) π-ferrosilicide reflection can initially be fitted well using an R3 unit cell, Figure 7 a-c, which by measuring the range in d-spacing between the two PV peaks, is found to be distorted such that $\alpha = \beta = \gamma = 89.75°$ at 410 MPa. At 979 MPa, it becomes clear that the peak shapes are best modelled using three PV functions, suggesting the transition to a P1

symmetry has occurred due to continued unit cell distortion. Modelling of the same (310) π-ferrosilicide diffraction peak using VESTA V3.3.2 (**Error! Reference source not found.**) revealed how the reduction in symmetry to a P1 space group setting leads to a similar effect as observed experimentally. For the purposes of the fitting using Fityk, the peaks were simplified to three PV peaks instead of the five demonstrated in the VESTA model. This process of comparison between the experimental data and the model, appeared to validate that the significant line broadening witnessed in the neutron diffraction datasets can be explained by a significant distortion of the π-ferrosilicide phase during mechanical loading. An angular range of possible α, β and γ values were calculated for the neutron diffraction data such that at 975 MPa (Figure 7d) α, β, γ = 90° to 89.62°. At 1692 MPa (Figure 7e) the distortion becomes more severe with: α, β, γ = 90° to 89.34°. Unfortunately, precise values of α, β and γ could not be determined due to the relatively low resolution of the diffraction peak. Therefore, it is not possible to determine a possible anisotropy for the three angles.

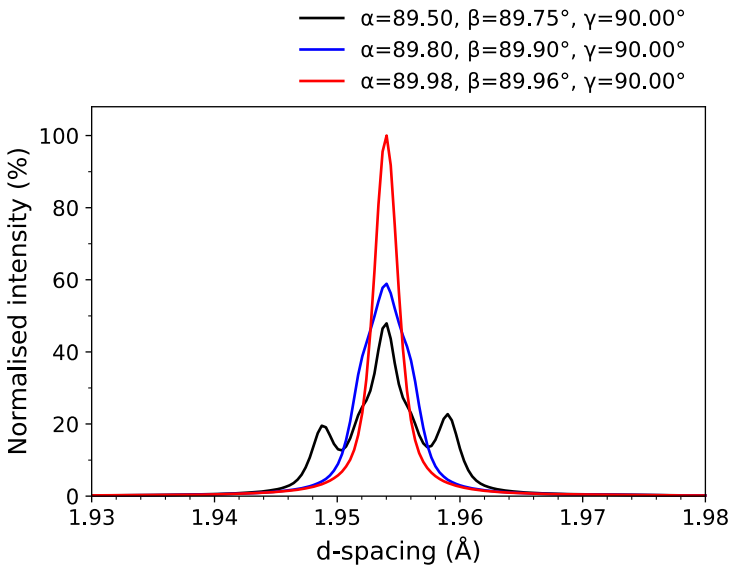

Figure 8. Simulated π-ferrosilicide (310) peak produced in VESTA showing the peak separation introduced by a strong unit cell distortion and subsequent reduction to P1 symmetry.

The detected distortion highlights that the π-ferrosilicide phase stores significant amounts of elastic energy during loading, which appears to be partially reversible (**Error! Reference source not found.**f). The surrounding austenite and ferrite, which clearly undergo significant plastic deformation (Figure 1b, Figure 4a & b, Figure 6), constrain the π-ferrosilicide upon unloading, preventing the complete reversal of the angular distortion. However, there will still be a very significant pull-back from the pure large-scale elastic response of the π-ferrosilicide upon unloading, particularly considering the strong bond between the π-ferrosilicide and the δ-ferrite due to their crystallographic relationship. It is proposed that in this way a substantial proportion of the relatively soft RR2450 matrix will remain resistant to galling.

From a galling perspective, the reinforcement of the matrix by this high strength π-ferrosilicide phase is a benefit. Typically, galling enhancement is made through precipitation strengthening [23] and increasing the matrix toughness [24]. As shown in Table 2, the RR2450 contains a significant proportion of carbide and carbonitride phases (28% in total) alongside 17% of the π-ferrosilicide phase. Effectively, these phases constitute hard-phase reinforcement in the RR2450 and account

for 45% of the overall microstructure. However, a great proportion of hard phases in the material can lead to significant embrittlement. Martensitic alloys have been shown to form a series of brittle cracks when loaded under wear conditions [25].

One way to mitigate against this, is to support hard phases in a softer matrix, such as austenite, to delay fracture [24]. To a degree, the RR2450 alloy offers this, as the softer austenite and ferrite phases account for over half of the microstructure. However, the π-ferrosilicide, despite being an incredibly strong phase, further exhibits a level of viscoelasticity by accommodating strain through the angular distortion of the unit cell, helping to prevent the compressive failure of the material. It can be assumed that this micromechanical aspect is an important factor in providing the excellent compressive loading performance observed for this alloy.

It is noted that the precise mechanism that gives rise to the angular distortion, and its increase in magnitude with progressive loading is not yet clear. It is evident that this avenue for further detailed mechanistic investigation should be explored to fully understand how such unusual behaviour could be better understood and potentially exploited in the future.

5. Conclusions

A complex multi-phase Fe-based alloy developed for improved galling wear resistance was investigated in terms of its micromechanics during compression loading. Two independent phase specific strain mapping techniques, neutron diffraction and SEM-based phase and DIC strain mapping, were utilised to obtain information on the elastic and plastic behaviour of the three main phases: austenite, d-ferrite and π-ferrosilicide, a highly complex hard phase. The main findings can be summarised as follows.

- The in-situ loading experiments using neutron diffraction show the expected load transfer from the soft austenite and δ-ferrite phases towards the hard π-ferrosilicide. However, the π-ferrosilicide reflection also develops very significant line broadening that far exceeds the observed line broadening of the two soft phases suggesting an additional deformation mechanism taking place in the π-ferrosilicide.
- The SEM-based local strain mapping approach shows no clear evidence of plastic strain within the π-ferrosilicide, confirming that dramatic peak broadening is not related to dislocation-based plasticity in this phase.
- Crystal structure modelling in combination with advanced peak fitting considering crystal distortion shows that an angular lattice cell distortion of <1° would account for the broadening observed during deformation in neutron diffraction. It is proposed that this visco-elastic behaviour of the π-ferrosilicide enables the storage of very high levels of elastic strain and in conjunction with the crystallographic relationship between π-ferrosilicide and δ-ferrite provides a pull-back mechanism upon unloading that explains the excellent compressive loading performance of RR2450.

Acknowledgements

We thank Rolls-Royce plc. and the Engineering and Physical Sciences Research Council (EPSRC) for financial support provided through the Advanced Metallic Systems Centre for Doctoral Training. MP also acknowledges his EPSRC Leadership Fellowship support

(EP/I005420/1) and NNUMAN (EP/J021172/1). DB and MP also acknowledge additional EPSRC funding (EP/R000956/1). We would like to acknowledge the support of ISIS Engin-X beamline staff, Dr. S. Kabra and Dr. J. Kelleher along with Dr. S. Irukuvarghula who provided support on the experiment and in discussions around the data analysis methodology. DB also acknowledges funding through the EPSRC Grant EP/T012250/1.

6. References

[1] I. Inglis, E. V. Murphy, H. Ocken, Performance of wear-resistant iron base hardfacing alloys in valves operating under prototypical pressurized water reactor conditions, Surf. Coatings Technol. 53 (1992) 101–106.
[2] H. Ocken, Reducing the Cobalt Inventory in Light Water Reactors., Nucl. Technol. 68 (1985) 18–28.
[3] D. Bowden, Y. Krysiak, L. Palatinus, D. Tsivoulas, S. Plana-Ruiz, E. Sarakinou, U. Kolb, D. Stewart, M. Preuss, A high-strength silicide phase in a stainless steel alloy designed for wear-resistant applications, Nat. Commun. 9 (2018) 1–10.
[4] D. Bowden, D. Stewart, M. Preuss, The identification of a silicide phase and its crystallographic orientation to ferrite within a complex stainless steel, J. Nucl. Mater. 517 (2019) 356–361.
[5] T. Ungár, Microstructural parameters from X-ray diffraction peak broadening, Scr. Mater. 51 (2004) 777–781.
[6] F. Di Gioacchino, J. Quinta da Fonseca, Plastic Strain Mapping with Sub-micron Resolution Using Digital Image Correlation, Exp. Mech. 53 (2013) 743–754.
[7] J.Q. Da Fonseca, P.M. Mummery, P.J. Withers, Full-field strain mapping by optical correlation of micrographs acquired during deformation, J. Microsc. 218 (2005) 9–21.
[8] M.A. Sutton, F. Hild, Recent Advances and Perspectives in Digital Image Correlation, Exp. Mech. (2015) 1–8.
[9] R. Thomas, D. Lunt, M.D. Atkinson, J. Quinta da Fonseca, M. Preuss, F. Barton, J. O'Hanlon, P. Frankel, Characterisation of irradiation enhanced strain localisation in a zirconium alloy, Materialia. 5 (2019) 100248.
[10] C. Zhao, D. Stewart, J. Jiang, F.P.E. Dunne, A comparative assessment of iron and cobalt-based hard-facing alloy deformation using HR-EBSD and HR-DIC, Acta Mater. 159 (2018) 173–186.
[11] W.B. Burdett, Hot isostatic pressing of hardfacing and stainless steel powders for PWR components-materials & manufacturing benefits, Am. Soc. Mech. Eng. Press. Vessel. Pip. Div. PVP. 6 (2012) 207–213.
[12] D. Bowden, D. Stewart, M. Preuss, Understanding the microstructural evolution of silicide-strengthened hardfacing steels, Mater. Des. 161 (2019) 1–13.
[13] J.R. Santisteban, M.R. Daymond, J.A. James, L. Edwards, ENGIN-X: A third-generation neutron strain scanner, J. Appl. Crystallogr. 39 (2006) 812–825.
[14] A.C. Larson, R.B. Von Dreele, Generalised Structure Analysis System, (1994).
[15] B.H. Toby, EXPGUI, a graphical user interface for GSAS, J. Appl. Crystallogr. 34 (2001) 210–213.
[16] M. Wojdyr, Fityk: A general-purpose peak fitting program, J. Appl. Crystallogr. 43 (2010) 1126–1128.
[17] K. Momma, F. Izumi, VESTA 3 for three-dimensional visualization of crystal, volumetric and morphology data, J. Appl. Crystallogr. 44 (2011) 1272–1276.
[18] M. Atkinson, R. Thomas, A. Harte, P. Crowther, J.Q. da Fonseca, DefDAP: Deformation Data Analysis in Python, Zenodo. (2020).
[19] F. Di Gioacchino, J. Quinta Da Fonseca, An experimental study of the polycrystalline plasticity of austenitic stainless steel, Int. J. Plast. 74 (2015) 92–109.
[20] S. Preibisch, S. Saalfeld, P. Tomancak, Globally optimal stitching of tiled 3D microscopic image acquisitions, Bioinformatics. 25 (2009) 1463–1465.
[21] D. Lunt, T. Busolo, X. Xu, J. Quinta da Fonseca, M. Preuss, Effect of nanoscale α2

precipitation on strain localisation in a two-phase Ti-alloy, Acta Mater. 129 (2017) 72–82.
[22] A. Orozco-Caballero, D. Lunt, J.D. Robson, J. Quinta da Fonseca, How magnesium accommodates local deformation incompatibility: A high-resolution digital image correlation study, Acta Mater. 133 (2017) 367–379.
[23] K.L. Hsu, T.M. Ahn, D.A. Rigney, Friction, wear and microstructure of unlubricated austenitic stainless steels, Wear. 60 (1980) 13–37.
[24] Ö.N. Doğan, J.A. Hawk, G. Laird, Solidification structure and abrasion resistance of high chromium white irons, Metall. Mater. Trans. A Phys. Metall. Mater. Sci. 28 (1997) 1315–1328.
[25] C. Allen, A. Ball, B.E. Protheroe, The Abrasive-Corrosive Wear of Stainless Steels, 74 (1981) 287–305.